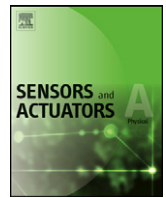




Contents lists available at [SciVerse ScienceDirect](http://SciVerse.ScienceDirect.com)

Sensors and Actuators A: Physical

journal homepage: www.elsevier.com/locate/sna



Driving high voltage piezoelectric actuators in microrobotic applications

Michael Karpelson*, Gu-Yeon Wei, Robert J. Wood

School of Engineering and Applied Sciences, Harvard University, United States

ARTICLE INFO

Article history:

Received 7 June 2011
Received in revised form 19 October 2011
Accepted 24 November 2011
Available online xxx

Keywords:

Piezoelectric actuators
Microrobotics
Power electronics
High voltage

ABSTRACT

Piezoelectric actuators have been used successfully to enable locomotion in aerial and ambulatory microrobotic platforms. However, the use of piezoelectric actuators presents two major challenges for power electronic design: generating high-voltage drive signals in systems typically powered by low-voltage energy sources, and recovering unused energy from the actuators. Due to these challenges, conventional drive circuits become too bulky or inefficient in low mass applications. This work describes electrical characteristics and drive requirements of low mass piezoelectric actuators, the design and optimization of suitable drive circuit topologies, aspects of the physical instantiation of these topologies, including the fabrication of extremely lightweight magnetic components, and a custom, ultra low power integrated circuit that implements control functionality for the drive circuits. The principles and building blocks presented here enable efficient high-voltage drive circuits that can satisfy the stringent weight and power requirements of microrobotic applications.

© 2011 Elsevier B.V. All rights reserved.

1. Introduction

Piezoelectric actuators hold promise for microrobotic applications due to high bandwidth, high power density, and the ability to scale to small sizes [1]. At the Harvard Microrobotics Laboratory, piezoelectric bending actuators have been used to enable locomotion in several robotic platforms, including a flapping-wing micro air vehicle (MAV) [2], a multi-segmented centipede robot [3], and a cockroach-inspired hexapod [4] (Fig. 1). However, the use of piezoelectric actuators is associated with two major challenges from a power electronics design standpoint.

Firstly, high voltages are required to generate sufficient force and displacement; for example, the actuators shown in Fig. 1 are driven in the range of 150–300 V. Most compact energy sources suitable for microrobotic applications, such as lithium batteries, supercapacitors, solar cells, and fuel cells, generate output voltages below 5 V, while connecting many such cells in series is usually not practical due to packaging overhead; this necessitates interface circuits with high voltage step-up ratios. Secondly, piezoelectric materials convert only a fraction of the input electrical energy into mechanical work, while the remainder is stored in the capacitive structure of the actuator and must be recovered to maximize system efficiency.

Prior work in high-voltage driving of piezoelectric actuators in microrobotic applications includes efforts by Steltz et al., which demonstrated a miniature voltage converter and a drive

stage with no energy recovery [5]. Campolo et al. proposed a charge recovery scheme for piezoelectric actuators using additional components [6], and Edamana et al. considered a similar scheme in a conceptual piezoelectric microrobot with a 20 V power supply [7]. However, the majority of existing publications focusing on efficient piezoelectric driving are targeted at large-scale, high-power (e.g. automotive, industrial, or naval) applications [8–11].

The overall goal of this paper is to describe circuit topologies that can overcome the challenges of low mass, high power density microrobotic applications, circuit control methods that maximize efficiency, and techniques to implement both the power circuits and the control functionality in an extremely lightweight package. Most of the analysis will focus on the flapping-wing platform of Fig. 1(a), which represents the most demanding weight and power requirements. Although this work focuses on piezoelectric actuators, many of the concepts described here can easily be adapted to other high-voltage capacitive actuators, such as electrostatic or dielectric elastomer actuators.

The paper begins by describing the electrical behavior and drive requirements of the actuators used in the platforms of Fig. 1. Two switching circuit topologies suitable for driving the actuators at high voltages using a low-voltage supply are presented, along with control methods that maximize efficiency for these topologies. The remainder of the paper focuses on the physical implementation of the drive circuits, including circuit optimization procedures with low computational requirements, fabrication of lightweight magnetic components and circuit assembly, and the design of a custom integrated circuit to implement the control functionality.

* Corresponding author.

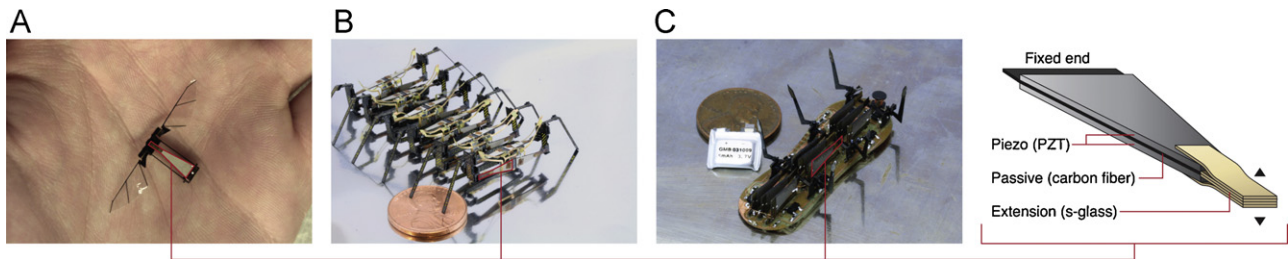


Fig. 1. Piezoelectric microrobots developed at the Harvard Microrobotics Laboratory: flapping-wing MAV (a), multi-segmented centipede robot (b), and cockroach-inspired hexapod (c). The structure of a piezoelectric bimorph actuator is also shown.

2. Piezoelectric actuators in the electrical domain

Piezoelectric actuators are available in many configurations, including stack actuators and bending devices such as unimorph and bimorph cantilevers. Bending actuators are generally more appropriate for applications that require strain amplification for large displacement (e.g. wing flapping or leg motion in a micro-robot). The actuator in Fig. 1 is a composite bimorph consisting of two PZT layers with plated nickel electrodes bonded to a central carbon fiber layer, with an s-glass extension. It is optimized for maximum energy density and designed to operate at fracture-limited electric fields, which, for the commercially available materials used, results in high drive voltages [1].

2.1. Drive requirements and methods

Traditional piezoelectric drive methods use an AC voltage source that causes the piezoelectric layer to expand and contract by the converse piezoelectric effect. Since the piezoelectric material is exposed to both positive and negative electric field with respect to its polarization direction (bipolar drive signal), depoling will occur if the field exceeds a certain threshold. However, to maximize energy density, it is desirable to expose the piezoelectric material to a field that will bring it close to fracture, which, for the actuators considered here, may be 4–6 times higher than the depoling threshold [1].

To prevent depoling, each piezoelectric layer must be kept under positive field with respect to polarization direction (unipolar drive signal). To drive a unimorph or other dual-electrode piezoelectric actuator under such constraints, a unipolar drive stage can be connected directly to the electrodes of the actuator, as shown in Fig. 2(a). Two methods of applying a unipolar drive signal to a bimorph are shown in Fig. 2(b) and (c). The method of Fig. 2(b), termed ‘alternating drive,’ comprises two unipolar drive stages connected to the outer electrodes and operated 180° out of phase, with a common ground on the central electrode. The method of Fig. 2(c), termed ‘simultaneous drive,’ comprises a constant high-voltage bias applied across the actuator and a unipolar drive stage connected to the central electrode. Alternating drive requires 2*n* drive stages per *n* bimorphs, while simultaneous drive allows sharing of the high-voltage bias between multiple actuators and therefore requires *n* drive stages and one bias per *n* bimorphs.

In addition to generating a unipolar drive signal, the drive stages must satisfy two important requirements. Firstly, they must be capable of generating arbitrary drive signal waveforms to maximize their versatility in different applications. Secondly, they must be capable of recovering unused electrical energy from the actuator to maximize system efficiency.

2.2. Electrical model

In order to design an efficient drive circuit, an electrical model of the load must be developed. The electrical response of a piezoelectric actuator varies both with the amplitude and the frequency of the drive signal. It is important to understand variation along both of these dimensions to ensure that the drive circuits can provide sufficient power to the actuator across the intended operating range.

In the frequency domain, a piezoelectric element can be represented with an equivalent circuit model where impedance reflects the dielectric and mechanical properties of the actuator and its load. A number of such models are described in literature, beginning with the Van Dyke model, described in the IEEE Standard on Piezoelectricity. Sherrit et al. developed an enhancement to the Van Dyke model that used complex values for the circuit components to better represent nonlinear losses in piezoelectric ceramics [12], while Guan et al. tried to approximate these losses with linear circuit components to draw more explicit parallels to the physical meanings of the circuit elements [13]. Other models, such as the ones described by Puttmer et al. [14] and Dahiya et al. [15], use a lossy transmission line to represent the mechanical domain, and either real or complex capacitances to represent the dielectric domain. In general, the models differ in (a) whether the mechanical domain is modeled using a lumped element model or a distributed model, and (b) whether they use linear or nonlinear circuit elements.

In this work, the mechanical domain is represented with a lumped element model, which has the advantage of simplicity over a distributed model and can be more easily related to linearized mechanical models [16]. The mechanical resonance modes are represented with a parallel combination of series LCR circuits, where inductance is related to mass, capacitance to compliance, and resistance to damping coefficient. The dielectric domain is represented with a complex capacitance, which is equivalent to a capacitor in parallel with a frequency-dependent resistor. The capacitance *C*₀

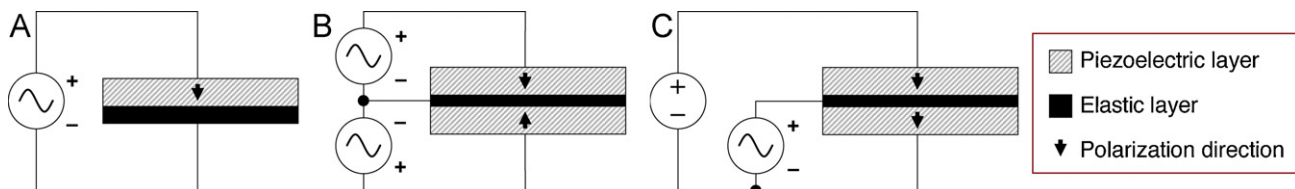


Fig. 2. Unipolar drive methods for optimal energy density piezoelectric actuators: unimorph (a), bimorph with alternating drive (b), and bimorph with simultaneous drive (c).

Table 1
Equivalent circuit parameters of bimorph actuator.

Drive voltage (V)	C_0 (nF)	$\tan(\delta)$	C_1 (pF)	L_1 (kH)	R_1 (M Ω)	C_2 (pF)	L_2 (kH)	R_2 (M Ω)
1	4.10	0.0117	88.0	29.6	1.66	15.0	30.5	2.55
20	4.31	0.0517	52.7	55	6.1	10.7	44	6.50
40	4.64	0.0838	58.8	55	8.2	11.1	44	10.1
60	4.84	0.1021	62.3	55	9.0	11.4	44	12.7
80	4.97	0.1125	63.7	55	9.0	11.7	44	13.4
100	5.04	0.1187	65.3	55	8.5	12.2	44	13.5

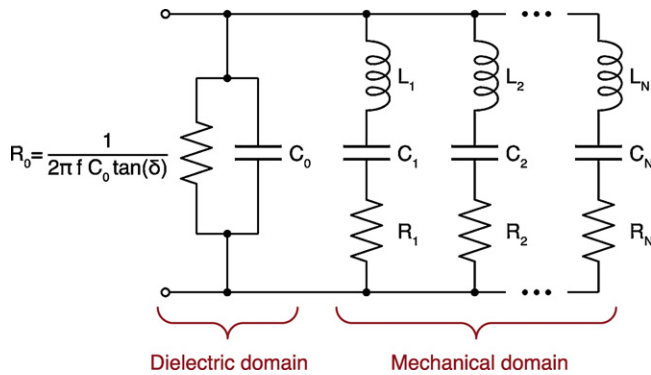


Fig. 3. Lumped element equivalent circuit representing a piezoelectric element.

arises from the structure of the piezoelectric element (two plated electrodes separated by a dielectric), while R_0 is a derived quantity representing various loss mechanisms in the dielectric. The complete equivalent circuit for a single piezoelectric element, shown in Fig. 3, can adequately represent a stack or unimorph bending actuator, or a single piezoelectric layer in a bimorph.

To extend the equivalent circuit model to the amplitude domain, the values of the circuit components in Fig. 3 can be parametrized with respect to drive signal amplitude. High-voltage characterization of a piezoelectric bimorph configured to drive the MAV of Fig. 1(a) was performed using a Newtons4th PSM1700 frequency response analyzer and a Trek PZD350 amplifier. PZT layers in the bimorph were machined from 127 μm Piezo Systems PSI-5H4E material. Fig. 4 shows the frequency response of one of the bimorph PZT layers and its equivalent circuit, with parameters fitted to the measured data, for several drive signal amplitudes (equivalent circuit parameters are given in Table 1, and the theoretical frequency response is calculated in MATLAB using the transfer function of the equivalent circuit). There are two prominent resonant modes: the first, at ~ 100 Hz, corresponds to wing flapping, and the second,

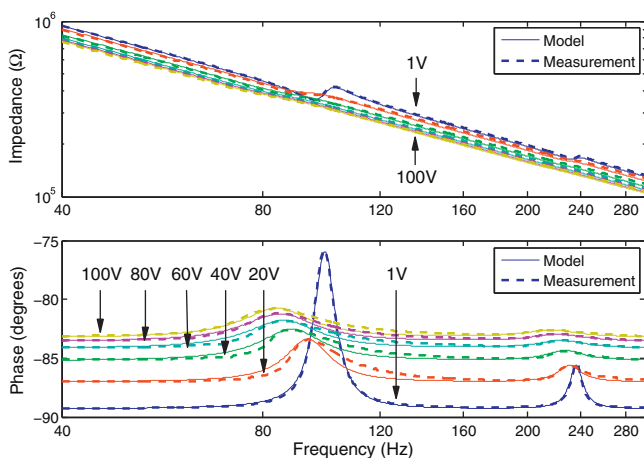


Fig. 4. Frequency response of a piezoelectric layer in a bimorph actuator.

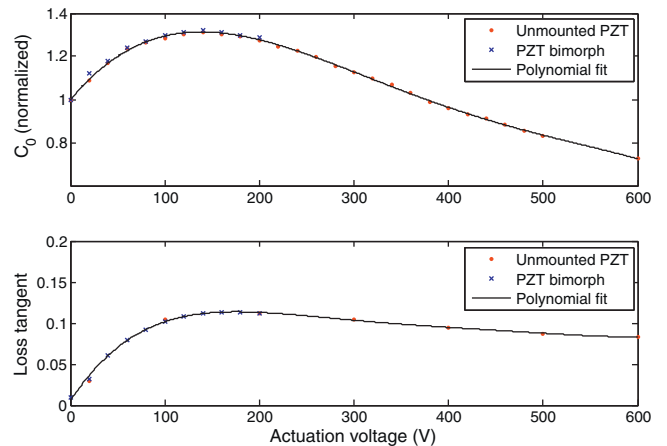


Fig. 5. Variation of equivalent circuit parameters with actuation voltage.

at ~ 230 Hz, corresponds to passive wing rotation (details on MAV design and resonant modes can be found in [2]). In this vehicle, the actuator is driven close to the first resonance mode to maximize wing stroke amplitude.

Most of the input electrical energy is stored in dielectric capacitance C_0 , and therefore the parameters C_0 and $\tan(\delta)$ (loss tangent) are of particular importance. Fig. 5 shows how these parameters change with drive voltage; results are provided for a bimorph actuator up to 200 V (corresponding to a field of ~ 1.58 V/ μm), and for an unmounted PZT sample up to 600 V (~ 4.72 V/ μm) to characterize behavior beyond the fracture limit of the bimorph. The capacitance C_0 is normalized to the value measured using small-signal (1 V) excitation. Also plotted is a 4th order polynomial fit for C_0 :

$$C_0 = C_L(A_4V^4 + A_3V^3 + A_2V^2 + A_1V + A_0) \quad (1)$$

where C_L is the value of C_0 as measured with small-signal excitation, and V is the drive voltage. A 5th order polynomial fit is used for $\tan(\delta)$:

$$\tan \delta = A_5V^5 + A_4V^4 + A_3V^3 + A_2V^2 + A_1V + A_0 \quad (2)$$

Coefficients A_N are different for capacitance and loss tangent data, and are provided in Table 2.

The values of the resonant components L_N , C_N , and R_N also change with actuation voltage; in particular, the resonant frequency tends to shift downwards due to the softening of PZT at high fields, represented by an increase in the compliance [1]. These variations can be parametrized in a manner similar to C_0 and $\tan(\delta)$

Table 2
Polynomial coefficients (Eqs. (1) and (2)).

Coefficient	C_0	$\tan(\delta)$
A_0	9.97467e-1	5.06029e-1
A_1	5.32173e-3	1.75419e-1
A_2	-2.79215e-5	-1.03013e-3
A_3	4.70610e-8	2.75369e-6
A_4	-2.76199e-11	-3.54923e-9
A_5		1.78257e-12

for a particular actuator-load configuration. However, for the system considered here, C_0 and $\tan(\delta)$ account for the majority of the electrical power draw during high voltage actuation, even when the system is driven at resonance; this is a natural consequence of the low electromechanical coupling coefficient in piezoelectric bending actuators [17].

3. Power circuit design

From a circuit design perspective, the drive circuits can be implemented in two fundamental ways: a dual-stage design, where a conversion stage steps up the low input voltage and a drive stage uses the conversion stage output to generate a time-varying drive signal; or a single-stage design, which simultaneously steps up the voltage and generates a drive signal. Since a dual-stage design inherently generates a regulated high voltage, it is well suited to the simultaneous drive method of Fig. 2(c), while a single-stage design is well suited for the alternating drive method of Fig. 2(b) and for dual-electrode actuators as in Fig. 2(a). A dual-stage design will generally have more components and greater weight, but will allow the high-voltage bias to be shared, while a single-stage design will be more lightweight but cannot be shared. As a result, the selection of the drive method will depend on the number and type of actuators in a given microrobotic platform.

Fig. 6 shows two switching power circuits – dual-stage and single-stage – that may be applied to the drive methods of Fig. 2, as well as the control architecture for both circuits, idealized switching waveforms, and an illustration of how the individual switching cycles combine to form steady-state behavior. The basic theory of operation for the two circuits is described below.

3.1. Dual-stage circuit

The conversion stage employs a topology known as the tapped inductor boost converter, which can be regarded as a combination of the well-known boost and flyback topologies and offers several advantages over other step-up topologies for low power, high voltage applications [18]. This design also lends itself well to miniaturization, which can reduce the efficiency and/or manufacturability of other topologies [19].

During a typical switching cycle, the switch Q (usually implemented as an nMOS or NPN transistor) is turned on, and current builds up in the primary winding L_p of the tapped inductor. When the current reaches the predetermined level I_{PKC} , Q is turned off, and the energy stored in the magnetic core ($L_p I_{PKC}^2 / 2$) is discharged to the high-voltage output through both the primary and the secondary windings. Further details on this topology can be found in [18].

The conversion stage operates in discontinuous mode, where the inductor current must return to zero before a new switching cycle may begin. This mode of operation is more efficient in low power, high step-up ratio converters, and simplifies the design of the control loop. In discontinuous mode, the voltage step-up ratio is given by:

$$\frac{V_B}{V_I} = \frac{V_I t_{on}^2}{2T I_B L_p} \quad (3)$$

where V_I and V_B are the input and output voltages, t_{on} is the on-time of the switch, T is switching period, and I_B is the load current.

The control functionality is achieved through pulse frequency modulation (PFM), represented by the ‘PFM controller’ block in Fig. 6(a). V_B is monitored using a resistive feedback divider and an analog comparator. When V_B falls beneath the regulation threshold, a switching cycle is initiated, delivering a quantity of energy to the output. PFM naturally adjusts the frequency of charging pulses

to regulate V_B at the desired level over a range of load currents, as illustrated in Fig. 6(c).

The half-bridge drive stage of the dual-stage design, found in many switching amplifiers, is a bidirectional switching topology that can both generate an arbitrary unipolar drive signal and recover energy from the load. When the high-side switch Q_H is turned on, the current in inductor L begins to rise. When the current reaches the predetermined level I_{PKdf} , Q_H is turned off, and the free-wheel current through diode D_L completes the delivery of energy to capacitive load C_{A1} , causing voltage V_O to rise. The change in V_O (ΔV_O) can be obtained from the energy balance equation:

$$\frac{L I_{PKdf}^2}{2} - E_{loss} = \frac{C_{A1}}{2} (V_O^2(\text{final}) - V_O^2(\text{initial})) \quad (4)$$

where E_{loss} is the energy dissipation in the drive circuit (discussed in more detail in Section 3.4), $V_O(\text{initial})$ and $V_O(\text{final})$ are the values of V_O at the beginning and end of the switching cycle ($\Delta V_O = V_O(\text{final}) - V_O(\text{initial})$), and all other quantities are as defined previously. Conversely, turning on the low-side switch Q_L and allowing the current in L to reach the value of $-I_{PKdf}$ recovers energy from C_{A1} and delivers it back to bias rail V_B via diode D_H , causing a decrease in V_O according to:

$$\frac{L I_{PKdf}^2}{2} - E_{loss} = \frac{C_{A1}}{2} (V_O^2(\text{initial}) - V_O^2(\text{final})) \quad (5)$$

By issuing a sequence of control signals to Q_H and Q_L , an arbitrary drive signal waveform can be generated at V_O , as shown in Fig. 6(c). When configured to drive a bimorph, represented by PZT elements C_{A1} and C_{A2} , the drive stage simply transfers charge between C_{A1} and C_{A2} , while the conversion stage provides energy to compensate for losses in the actuator and the drive stage.

The conventional approach to switching amplifiers uses the switches to generate a pulse width modulation (PWM) signal, which is converted by an LC network into an output voltage equal to the average value of the PWM signal. When connected to a capacitive load with significant energy storage, such as a piezoelectric actuator, the amplifier must actively charge and discharge the load during each switching cycle. This results in significant switching losses even when the output voltage is relatively constant or cycling at low frequency.

Janocha and Stiebel proposed a control method where the switches remain idle unless energy needs to be transferred to or from the load, reducing switching losses significantly [20]. A modified version of this method is embodied in this work through a four-phase control algorithm—*Acquisition*, *Lookup*, *Charge*, and *Discharge*. The associated control architecture is shown in Fig. 6(a).

During *Acquisition*, the voltage V_O is sampled using an analog-to-digital converter (ADC). In the *Lookup* phase, the ADC result, along with digital signal V_{CTRL} (the desired value of V_O) are used to address a lookup table (LUT) that stores on-times for switches Q_H and Q_L . Because the parameters of the actuator and the drive circuit are known in advance, it is possible to precompute the on-times according to the standard inductor equation:

$$t_{onH} = \frac{L I_{PKdf}}{V_B - V_O}, \quad t_{onL} = \frac{L I_{PKdf}(V_O)}{V_O} \quad (6)$$

Here, I_{PKdf} and I_{PKdr} are functions of V_O , and can be constrained according to Eqs. (4) and (5) to ensure that the generated drive signal meets desired specifications for minimum and maximum slew rate (ΔV_O per unit time).

During the *Charge* phase, a timing pulse generator turns on the appropriate switch for the prescribed length of time, initiating the transfer of energy to or from node V_O . Finally, during the *Discharge* phase, the switch is turned off, and the energy transfer is completed via one of the freewheel diodes, thereby raising or lowering the voltage V_O . A current sense circuit detects when the current in L has

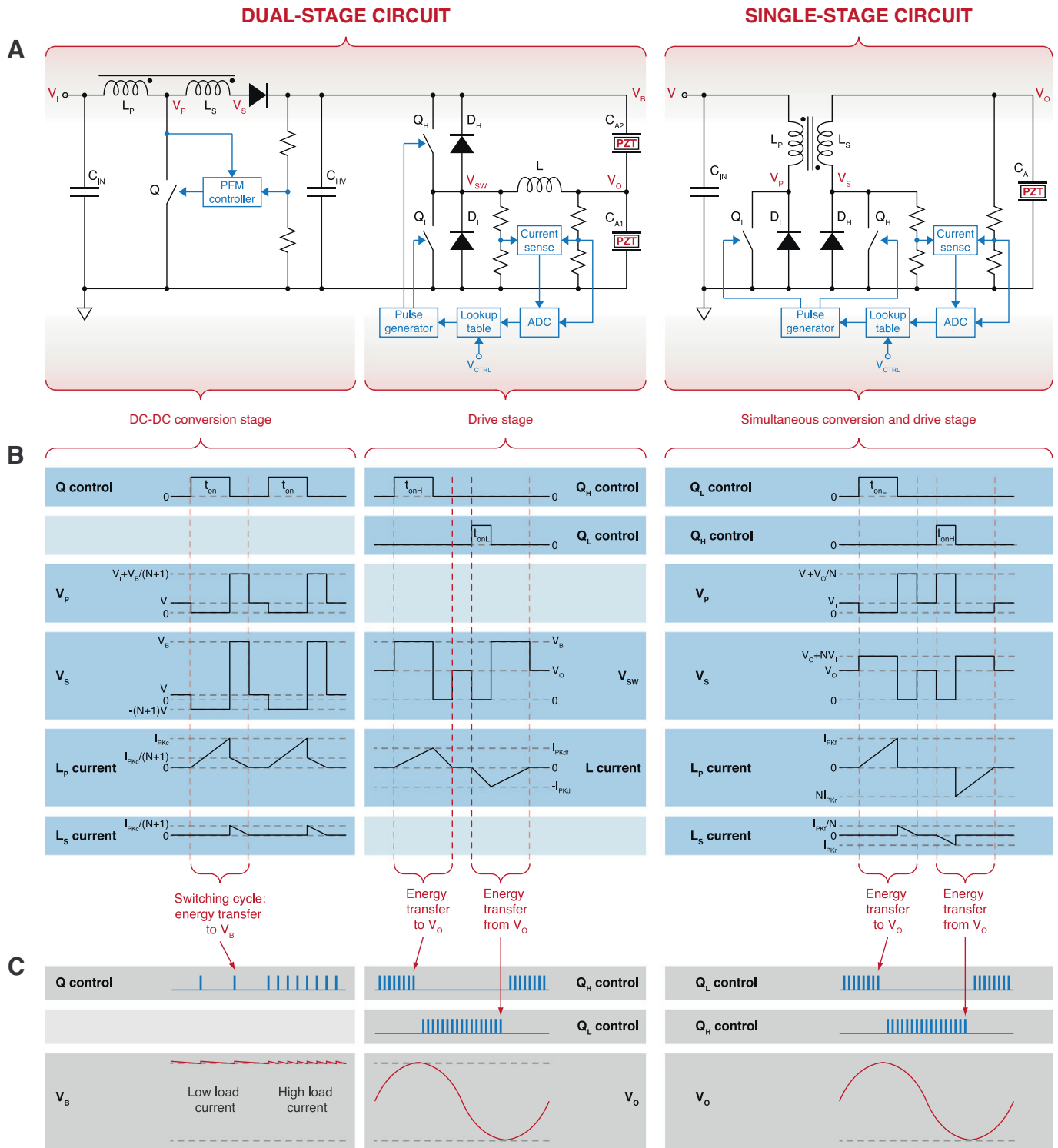


Fig. 6. Piezoelectric drive circuits and control architecture (a), switching waveforms (b), and steady-state operation (c).

returned to zero, indicating that it is safe to begin a new Acquisition phase. Through successive iterations of the four phases, V_O is driven towards its desired value V_{CTRL} .

3.2. Single-stage circuit

The single-stage drive circuit in Fig. 6 is a bidirectional flyback converter, which shares many advantages with the tapped inductor boost converter described in the previous section. To transfer energy to the load, Q_L is turned on, causing the current in the

primary winding L_P of the flyback transformer to rise to predetermined level I_{PKf} . When Q_L is turned off, the energy in the transformer core is discharged into capacitive load C_A via secondary winding L_S and diode D_H , causing output voltage V_O to rise. The change in V_O (ΔV_O) can be obtained from the energy balance equation, as before:

$$\frac{L_P^2 I_{PKf}^2}{2} - E_{loss} = \frac{C_A}{2} (V_O^2(\text{final}) - V_O^2(\text{initial})) \quad (7)$$

where E_{loss} is the energy dissipation in the drive circuit, $V_{\text{O}}(\text{initial})$ and $V_{\text{O}}(\text{final})$ are the values of V_{O} at the beginning and end of the switching cycle, and all other quantities are as defined previously. Q_{H} and D_{L} are used in a similar fashion to lower V_{O} via secondary winding L_{S} :

$$\frac{L_{\text{S}} I_{\text{PKr}}^2}{2} - E_{\text{loss}} = \frac{C_{\text{A}}}{2} (V_{\text{O}}^2(\text{initial}) - V_{\text{O}}^2(\text{final})) \quad (8)$$

By timing the control signals appropriately, the bidirectional flyback converter can generate an arbitrary drive signal waveform and recover unused energy from the actuator, similar to the half-bridge drive stage (Fig. 6(c)). Note that the functions of the low-side and high-side switches are reversed, meaning that Q_{L} is used during energy transfer from supply to load, while Q_{H} is used during energy transfer from load to supply. Further details on this topology may be found in [21].

The control method of the bidirectional flyback converter is identical to the one used in the half-bridge drive stage, allowing the same hardware to be used for either design; the only difference lies in the precomputed values stored in the LUT. The on-times can be calculated according to:

$$t_{\text{onL}} = \frac{L_{\text{p}} I_{\text{PKr}}(V_{\text{O}})}{V_{\text{I}}}, \quad t_{\text{onH}} = \frac{L_{\text{s}} I_{\text{PKr}}(V_{\text{O}})}{V_{\text{O}}} \quad (9)$$

where all quantities are as defined previously.

3.3. Custom magnetics and circuit assembly

Magnetic components are central to the implementation of the circuits in Fig. 6. Although there is a wide range of commercially available mg-scale magnetic components, very few are intended for high-voltage or high step-up ratio applications. For example, as of this writing, the smallest available flyback transformer with a sufficient turns ratio for use in the topologies of Fig. 6 (Coilcraft LPR4012 series) weighs 54 mg, or almost the entire weight of the MAV in Fig. 1(a). Two approaches have been used successfully to implement magnetics for the circuits of Fig. 6: ferrite bobbin cores salvaged from commercial inductors and E-cores fabricated using laser micromachining [22].

Laser ablation is a rapid and non-contact method of patterning and cutting ferrite materials [23], making it a promising method for machining planar ferrite cores of arbitrary geometry. In particular, E-cores are an attractive alternative to bobbin cores, as they are simple to machine from planar sheets of ferrite, allow for precise control of inductance, and enable good magnetic coupling between windings. Although E-cores are not fully self-shielding, they also have better electromagnetic interference (EMI) characteristics than unshielded bobbin cores. EMI can affect the operation of noise-sensitive circuits, such as sensor interfaces, as well as nearby power circuits; this is particularly significant in micro-robotic applications, where multiple circuits are likely to be in close proximity. To manufacture inductors and tapped inductors/flyback transformers, an air gap is introduced by shortening the center leg of the E. Unlike a bobbin core, this configuration places the air gap in the middle of the coil, which reduces EMI.

A diode-pumped solid-state (DPSS) laser micromachining system is used to fabricate gapped E-cores from sheets of ferrite that have been lapped down to a required thickness. With refocusing, the laser can cut samples over 500 μm in thickness. Fig. 7 illustrates the custom magnetics fabrication process. The coils are wound on temporary bobbins formed using Kapton liner and laser-cut plastic discs, and the windings are cemented with cyanoacrylate adhesive. The temporary bobbin is removed, and two laser micromachined E-cores are inserted manually into the windings using an optical microscopy station and glued together. This

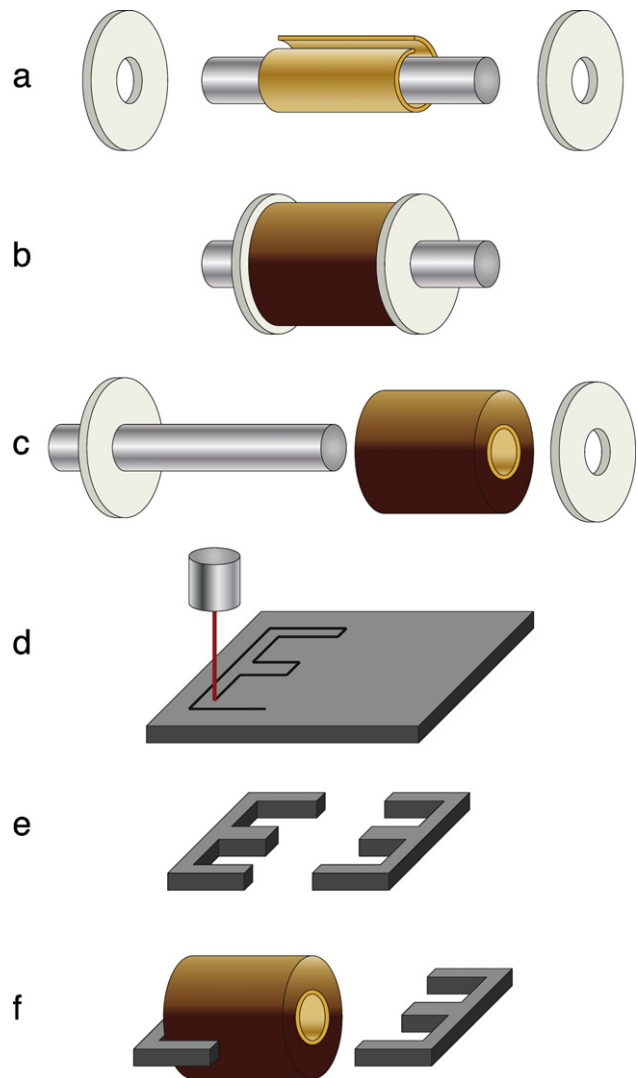


Fig. 7. Fabrication of custom magnetic components: (a) temporary bobbin formation using Kapton liner and laser-cut plastic discs, (b) coil winding, (c) temporary bobbin removal, (d) laser micromachining of ferrite core, (e) core release and (f) component assembly.

manufacturing method can yield ferrite structures with 10 μm resolution and has been used to create magnetic components weighing 5–20 mg.

Surface-mount capacitive and resistive components have low packaging overhead, and therefore it is difficult to reduce their weight further. In semiconductors, however, packaging overhead frequently exceeds 90% of total weight, making it highly desirable to use bare die or chip-scale components. Furthermore, the circuit substrate can account for a significant percentage of the weight in mg-scale devices. Although flexibility is not always a requirement, flexible circuits manufactured by applying conventional circuit lithography to copper-laminated polymer films (e.g. DuPont Pyralux) can produce circuit substrates weighing as little as 5 mg/cm². In this work, circuit lithography and machining are also performed using DPSS laser micromachining. Circuit components are positioned on the substrate and undergo either manual or reflow soldering.

Fig. 8 shows a range of components that can be used to implement the circuits of Fig. 6; also shown are laser micromachined E-cores and bobbin cores salvaged from commercial inductors.

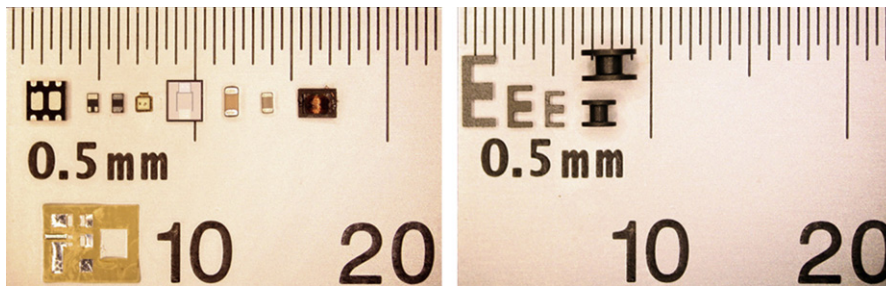


Fig. 8. Circuit components and ferrite cores. Top left: chip scale and bare die transistors, chip capacitors, custom inductor. Bottom left: flex substrate. Right: laser micromachined gapped E-cores and commercial bobbin cores.

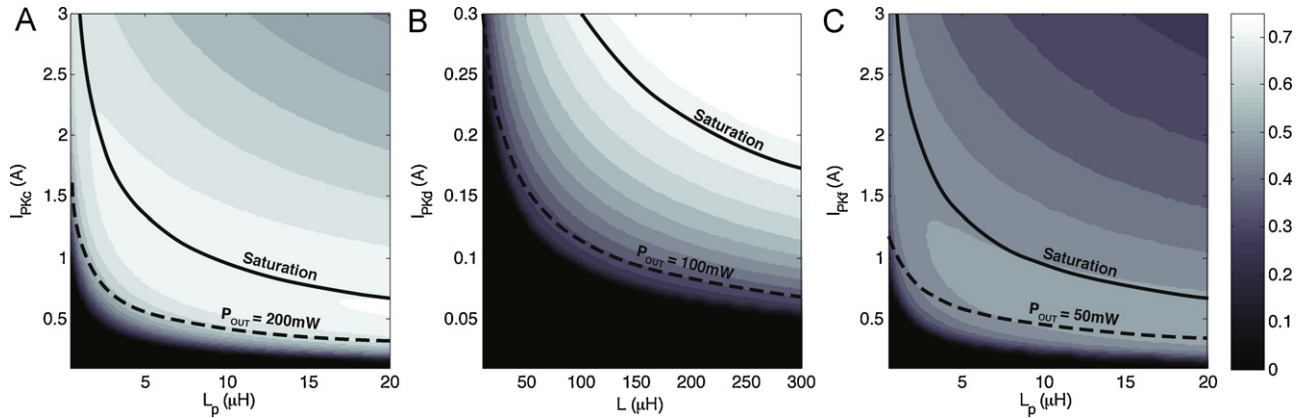


Fig. 9. Contour plots of efficiency vs. peak current and inductance for tapped inductor boost converter (a), half-bridge drive stage (b), and bidirectional flyback drive stage (c). Solid lines indicate the saturation limit of a typical mg-scale ferrite core, and dashed lines are examples of minimum output power constraints for each topology.

3.4. Circuit modeling and optimization

The design and optimization of switching power supplies generally involves the use of SPICE software tools to verify circuit operation and estimate efficiency prior to hardware implementation. However, SPICE simulation can be computationally demanding, particularly when it is necessary to examine a large design space, which, for the power circuits of Fig. 6, includes not only circuit design parameters, such as peak current values and winding ratios, but also the wire gauges of each winding and the parameters of the semiconductor devices used in each design. In the case of custom magnetic components, the design space also includes the geometric parameters of the core and ferrite material properties. Finally, using SPICE to estimate the efficiency of a drive stage involves simulating at least one full period of the output signal, which is itself composed of up to several thousand individual switching cycles (see conceptual illustrations in Fig. 6(c)).

To perform a high-level optimization of the power circuits without the computational burden of SPICE simulation, a series of MATLAB scripts is developed to model loss mechanisms as a function of design parameters. The losses can be broadly categorized as conduction losses, which include the switch on-state resistances, the diode forward voltage drop, and the series resistances of magnetic components; switching losses, which include the energy required to charge the gate and output capacitances of the switches, switch turn-on and turn-off losses, and diode recovery losses; and finally, magnetic losses, which include hysteresis losses, eddy current losses, and leakage inductance. Closed-form estimates for these loss mechanisms are discussed extensively in literature and electronics texts (e.g. Pressman [24]). Auxiliary MATLAB models are used to estimate relevant parameters for custom magnetic components based on geometry, number of turns in a winding, wire gauge, and core material properties. Although the MATLAB approach is not as accurate as SPICE simulation (or finite

element modeling in the case of magnetic components), it provides an accurate representation of the relative performance of various designs and can be used to narrow the design space significantly before moving to more accurate but computationally expensive modeling techniques.

The primary purpose of the MATLAB models is to permit a fast optimization of the power circuits for efficiency, subject to design constraints. For a unidirectional circuit, such as the tapped inductor boost converter, the efficiency calculation is straightforward:

$$\eta = \frac{P_{out}}{P_{in}} = \frac{V_B I_B}{V_I I_I} \tag{10}$$

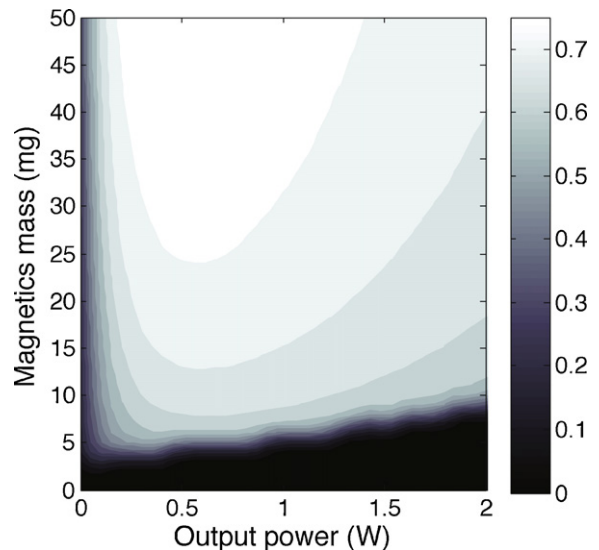


Fig. 10. Contour plot of efficiency vs. output power and magnetics mass for the tapped inductor boost converter.

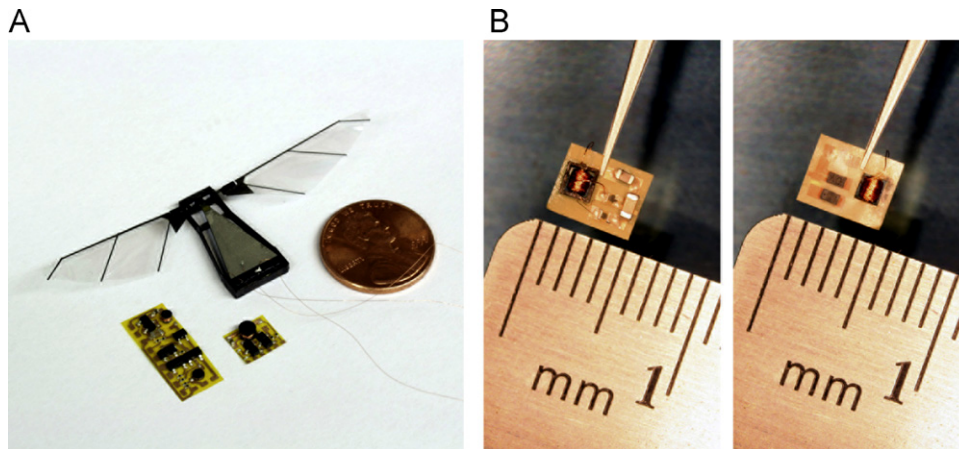


Fig. 11. (a) Previous implementations of piezoelectric drive circuits next to a scaled-up version of the MAV of Fig. 1. (b) Front and back view of 20 mg tapped inductor boost converter.

where P_{out} and P_{in} are the output and input power, and I_B and I_l are the load and input currents. For the two drive stages, which rely on bidirectional power transfer, efficiency is calculated by assuming an ideal capacitive load C connected to node V_O , in order to decouple circuit losses from actuator losses:

$$\eta = \frac{P_{out}}{P_{loss} + P_{out}} = \frac{C \max(V_O^2)/2}{P_{loss}/f + C \max(V_O^2)/2} \quad (11)$$

where P_{out} is the power delivered to the output, P_{loss} is the power dissipated in the drive stage, f is the drive signal frequency, and $\max(V_O)$ is the drive signal amplitude.

The MATLAB models can also be used to obtain insight into the scaling of loss mechanisms and tradeoffs between various design parameters. Figs. 9 and 10 give two examples of useful data that can be extracted. Note that the MATLAB code used to produce these plots runs in several minutes on a typical desktop computer (2.3 GHz processor, 4GB RAM), while equivalent SPICE and FEM simulations would take many hours on similar hardware.

Fig. 9 shows the efficiency of the power circuits in Fig. 6 in the space of two design parameters: peak current and inductance. Solid lines indicate the saturation limits for a typical mg-scale ferrite core; above the lines, the core cannot store any more energy and enters saturation. Dashed lines indicate output power constraints; below the lines, the core stores too little energy, and the circuit cannot provide sufficient output power (the values in Fig. 9 are examples only and not based on a particular actuator geometry or drive conditions). The safe operating regions therefore lie between the solid and dashed lines.

The data in Fig. 9 gives insight into the dominant loss mechanisms of the power circuits. For example, the tapped inductor boost converter in Fig. 10(a) and the bidirectional flyback drive stage in Fig. 10(c) provide maximum efficiency in a region somewhere between the saturation and power limits—here, the various loss mechanisms are balanced. The half-bridge drive stage in Fig. 10(b), by contrast, exhibits the characteristic behavior of a circuit where switching losses dominate. Regions of high efficiency lie close to the core saturation limit, because transferring the maximum possible amount of energy during each switching cycle minimizes the overall number of switching cycles, and therefore energy loss.

Fig. 10 illustrates some of the tradeoffs between the maximum output power, efficiency, and mass for a laser micromachined magnetic core (the tapped inductor boost converter is used in this example, but other designs exhibit similar trends). Since, for a given power level, circuit efficiency can be increased at the cost of magnetics mass, data like this may be used to determine whether, for a given robotic platform, it is more beneficial to use a larger, more

efficient magnetic core or to select a smaller core and make up for reduced efficiency by allocating more of the weight budget to the battery.

4. Physical instantiation

In previous work, the circuits of Fig. 6 were implemented using conventionally packaged discrete components and custom-wound bobbin cores on a flex substrate (Fig. 11(a)) [19]. The dual-stage design weighed 90 mg, comprising a 40 mg conversion stage and a 50 mg drive stage, and the single-stage circuit weighed 60 mg (not including control functionality). Since then, a growing number of high-voltage components in chip-scale packaging have appeared on the market. This, along with the laser micromachined magnetic components described in Section 3.3, presents an opportunity for further weight reduction. The tapped inductor boost converter is selected here as a representative topology to demonstrate the potential for improvement.

Three versions of the tapped inductor boost converter are designed. The first two versions weigh 40 mg and serve to compare the performance of laser micromachined magnetics to bobbin-core devices of equal mass, while the third version uses laser micromachined magnetics and weighs 20 mg (Fig. 11(b)). Control functionality remains external for all three designs and is implemented using an Atmel AVR microcontroller. The bobbin core is obtained from the Coilcraft LPS3015 series of power inductors, while the E-cores are machined using 8040 ferrite from TSC Ferrite International. All three designs are optimized using the MATLAB models described in Section 3.4. The components of the three designs are summarized in Table 3 (the predicted values of some parameters, obtained from the MATLAB model, are also provided).

Fig. 12 shows relative EMI measurements obtained by placing an unshielded coil 1 cm away from the bobbin and E-core magnetic devices in the same position and orientation, similar to the method of [25]. Both converters are switching at 150 kHz during the measurement. This result illustrates the shielding advantage of an E-core, which significantly reduces EMI at the switching frequency and its harmonics. However, measurements also indicate that laser micromachined cores exhibit significantly higher magnetic core losses (up to 50 times the expected value), which translates into a 5–10% efficiency penalty for the circuits considered here. The increase in magnetic losses has been quantified by measuring the efficiency of two converters where all circuit components are identical and all tapped inductor parameters are matched as closely as possible, except for the core type. The changes in ferrite properties

Table 3
Converter design parameters (predicted values given in parentheses where appropriate).

Converter design	1	2	3
Minimum output power (200 V)	200mW	200 mW	60 mW
Converter mass ^a	40 mg	40 mg	20 mg
Switch	Zetex ZXMN6A07F	Zetex ZXMN6A07F	Zetex DMN3730UFB
Diode	Zetex BAW101S	Zetex BAW101S	Zetex BAS521LP
Core type	Bobbin	Gapped E-core	Gapped E-core
Tapped inductor mass	15 mg	15 mg	8 mg
Turns ratio	6.9	6.8	8.15
Primary inductance	6.20 μ H	6.63 μ H (6.44 μ H)	2.54 μ H (2.2 μ H)
Secondary inductance	300 μ H	309 μ H (315 μ H)	169 μ H (147 μ H)
Primary resistance	1 Ω	0.75 Ω (0.68 Ω)	0.87 Ω (1.02 Ω)
Secondary resistance	42.7 Ω	44.3 Ω (49.4 Ω)	29.8 Ω (34.4 Ω)
Coupling coefficient	0.92	0.95	0.84

^a Excluding control functionality.

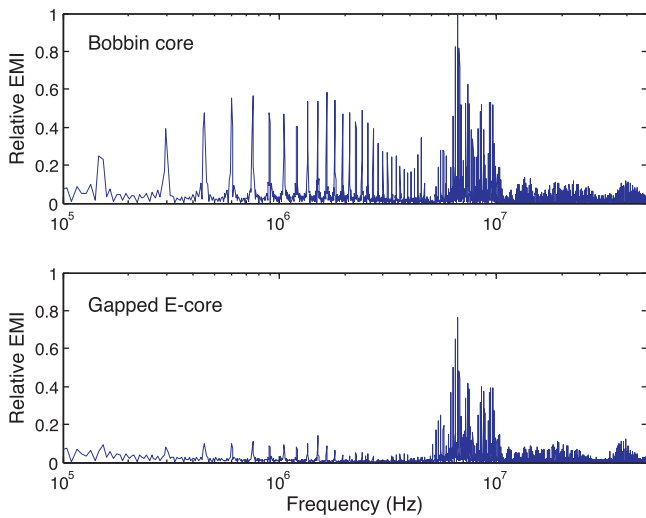


Fig. 12. Relative EMI spectra measured 1 cm from bobbin core and gapped E-core.

are thought to be caused by excessive local heating during the laser micromachining process [22].

The loss mechanisms calculations in the MATLAB models are based on worst-case conditions, and therefore measured efficiency is typically higher than predicted by the model. However, the relative efficiency values are consistent across different designs. Fig. 13 shows the measured efficiency vs. output power for the three converters. Also shown are theoretical efficiency curves, obtained from the MATLAB model, where the energy loss estimates are scaled by the same factor for all three designs. The models have also been modified to account for increased core loss in laser micromachined components. Table 4 provides additional performance metrics for the three designs.

4.1. Integrated control circuit

To enable a fully autonomous power electronics package, the control functionality described in Sections 3.1 and 3.2 needs to

Table 4
Conversion stage performance.

Converter design	1	2	3
Maximum efficiency (200 V)	72%	69%	52%
Maximum efficiency (150 V)	75%	77%	59%
Maximum output power (200 V)	310 mW	210 mW	68 mW
Maximum output power (150 V)	390 mW	250 mW	82.5 mW
Power density (200 V)	7.75 kW/kg	5.25 kW/kg	3.4 kW/kg
Power density (150 V)	9.75 kW/kg	6.25 kW/kg	4.13 kW/kg

be implemented in a compact package with ultra-low power consumption in order to have a negligible effect on both the mass and the overall efficiency of the drive circuits. A custom integrated circuit (IC) is an obvious choice to meet these requirements.

The control IC is designed in 0.13 μ m CMOS technology and contains two channels that share a current reference, a control register bank, and a serial programming interface. Fig. 14 shows a block diagram of a single channel, along with shared components. Per the simplified depiction of the control architecture given in Fig. 6, each channel includes an ADC, a LUT, pulse generation logic, and a current sense circuit. Each channel can control either one of the drive stages described in Fig. 6 by programming appropriate values into the LUT. However, the IC does not implement the PFM controller block from the conversion stage of Fig. 6; PFM controllers, with and without integrated power switches, are well documented in literature and widely available commercially, and are therefore outside the scope of this work.

The ADC is implemented using a Successive Approximation Register (SAR) architecture and is capable of up to 200 kSps at a selectable resolution of 6–8 bits. Since, in most cases, V_O changes by less than 2 ADC least significant bits (LSBs) between successive Acquisition phases, built-in ADC logic records the previous conversion value and operates as a delta-encoded ADC at the beginning

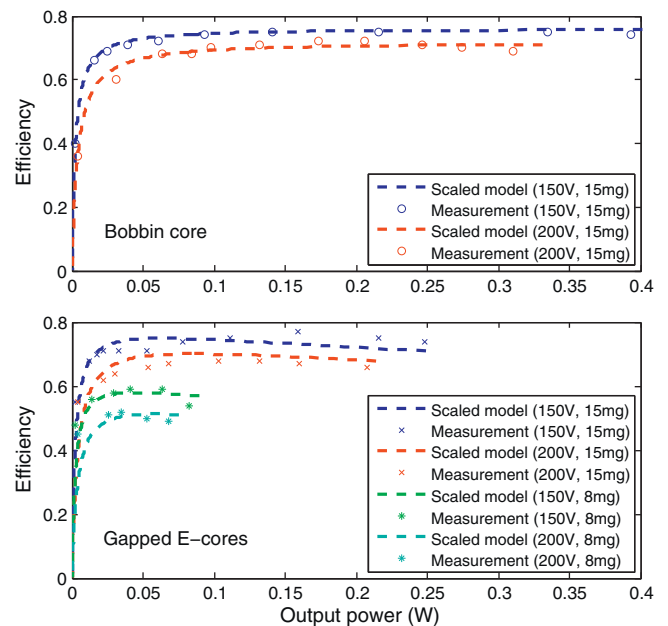


Fig. 13. Efficiency vs. output power of tapped inductor boost converters using bobbin cores and laser micromachined E-cores (legend indicates output voltage and tapped inductor mass).

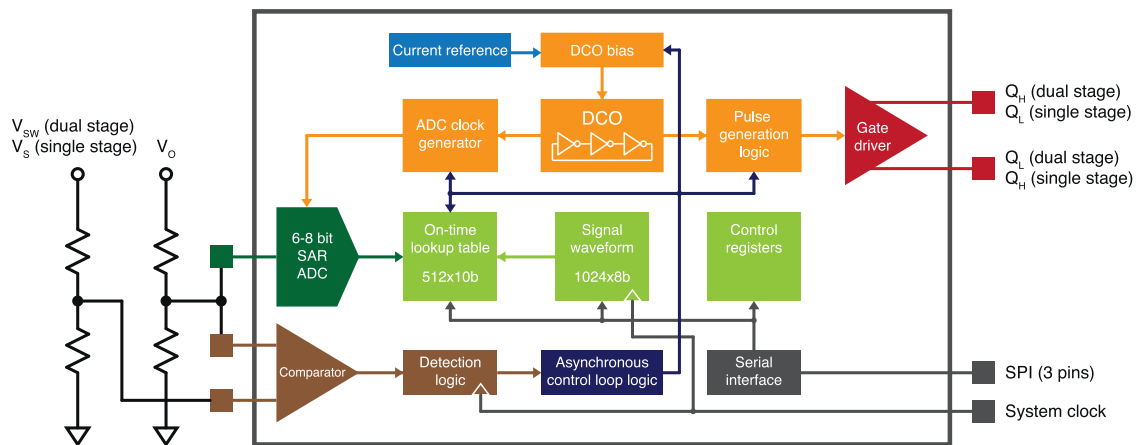


Fig. 14. Block diagram of single channel (I/O labels correspond to Fig. 6).

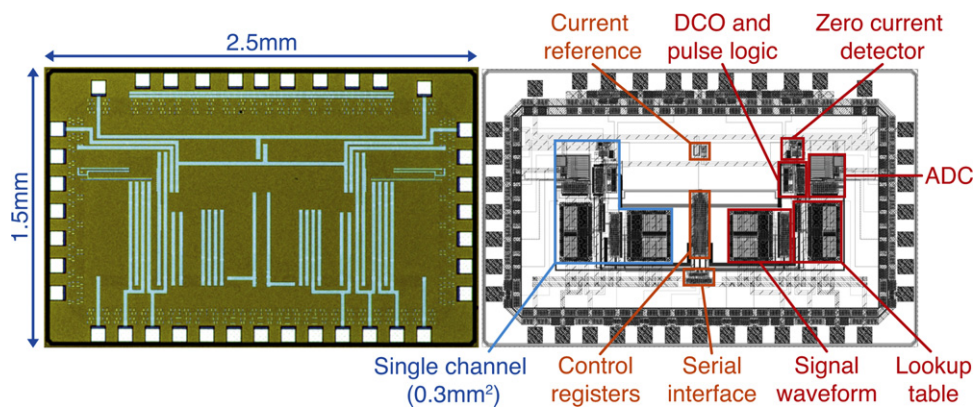


Fig. 15. Die photograph (left) and diagram (right). In the photograph (left), the top-level metal layer obscures the internal IC structure.

of each new *Acquisition* phase. This reduces ADC conversion time to 2–4 ADC clock cycles. If the delta-encoded search fails due to an abnormal event (e.g. a voltage transient due to external stimulation of the actuator) the ADC reverts to a binary search algorithm, more typical of SAR ADCs, after a selectable number of cycles (up to 8).

The LUT is implemented using a 512 × 10 bit SRAM. A second 1024 × 8 bit SRAM stores (optionally) drive signal waveforms (i.e. sequences of V_{CTRL}) to facilitate testing; in a fully autonomous robotic platform, the V_{CTRL} signal would be provided by a higher-level microprocessor “brain.”

The current sense circuit detects when inductor (or flyback transformer) current has reached zero by using a rail-to-rail comparator that monitors the voltages at the terminals of the winding

(secondary winding in the case of the flyback transformer); this allows a new *Acquisition* phase to commence. If the comparator fails to trigger, a fail-safe timer kicks the controller into the *Acquisition* phase after an appropriate amount of time.

The control algorithm imposes many timing requirements, including generating precise timing pulses in the *Charge* phase and providing a clock for the ADC. To allow inductor current i to reach the correct level in conditions of high di/dt (short pulses), 10 ns resolution is required for the circuits considered in this work. Lower resolution is acceptable at lower di/dt (longer pulses). During *Charge*, a wide tuning range digitally-controlled oscillator (DCO) operates at 50 MHz with 50% duty cycle, allowing for 10 ns resolution, and at 25 MHz at low di/dt conditions to reduce power consumption. During *Acquisition*, the DCO operates at 5 MHz and is further divided down to generate the ADC clock. The DCO is disabled from the end of the *Charge* phase until the next *Acquisition* phase.

The control loop logic relies on S–R latches to enable a semi-asynchronous architecture that, along with the variable-speed DCO, provides high temporal resolution without the need for a

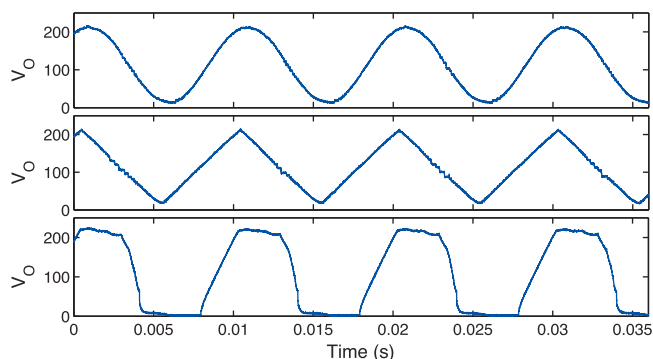


Fig. 16. Scope traces of three different drive signal profiles on V_O (sinusoidal, triangular, and square wave).

Table 5
Control IC power measurements.

Current reference	8.9 μ W
DCO (5 MHz)	79 μ W
DCO (50 MHz)	732 μ W
Zero current detector	11 μ W
Leakage power (2 channels)	21 μ W
ADC (8-bit mode)	3.2 μ W
Aggregate (single channel)	60 μ W
Aggregate (dual channel)	98 μ W

Table 6
Drive stage efficiency.

	Half-bridge drive stage		Bidirectional flyback drive stage	
High-side switch	Zetex ZXMP2120E5 pFET		Vishay TN2404 K nFET	
Low-side switch	Vishay SiA950DJ nFET		Infineon BSS670S2L nFET	
Magnetics	Inductor, $L = 300 \mu\text{H}$		Flyback transformer, $L_p = 6 \mu\text{H}$, $N = 6$	
Drive frequency, load	Predicted efficiency	Measured efficiency	Predicted efficiency	Measured efficiency
100 Hz, 10 nF	47.9%	52.3%	42.8%	48.3%
100 Hz, 20 nF	51.0%	54.9%	45.0%	52.1%
100 Hz, 30 nF	51.7%	55.1%	45.7%	52.3%
200 Hz, 10 nF	50.9%	52.9%	45.0%	51.5%
200 Hz, 20 nF	52.5%	54.3%	45.6%	52.9%
300 Hz, 10 nF	52.6%	53.9%	45.7%	53.3%

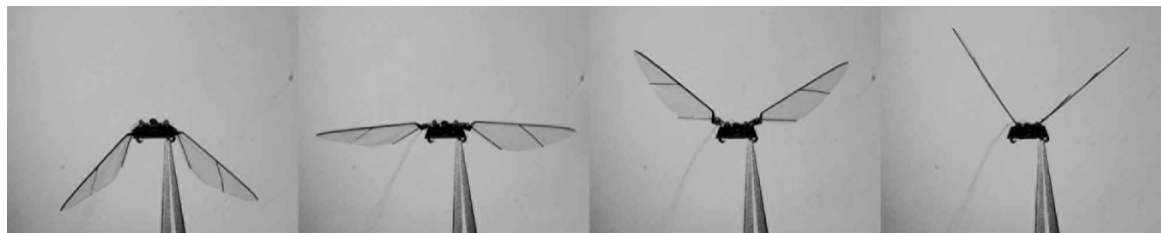


Fig. 17. High-speed video frames of robotic insect wings flapping at 100 Hz.

global high-speed clock. When the optional signal waveform SRAM is used, a sub-100 kHz external clock is required for accurate timing of the stored V_{CTRL} sequence.

To reduce switching losses (e.g., due to ADC error), an optional mode keeps track of previous V_{CTRL} samples and suppresses pulses that would lower V_O during periods when V_{CTRL} is monotonically increasing or, conversely, pulses that would increase V_O when V_{CTRL} is monotonically decreasing. This reduces errant switching pulses, but also reduces the capability of the controller to compensate for unexpected changes in V_O .

The dual-channel control IC occupies 0.66 mm^2 ($2.5 \times 1.5 \text{ mm}$ total die size). The die photograph and layout are shown in Fig. 15. When driving an actuator with a 100 Hz sinusoidal signal, the IC consumes less than $50 \mu\text{W}/\text{channel}$ during dual-channel operation at 1.0V supply. Table 5 lists the power consumption of individual blocks and operating modes. Despite the high power draw of the DCO at 50 MHz, incorporating lower-frequency operating modes

and disabling the DCO when not in use results in low aggregate power consumption.

Fig. 16 shows three different drive signal profiles measured while using the control IC and the half-bridge drive stage to drive an ideal capacitive load representing a piezoelectric bimorph. The third waveform (square wave) illustrates the finite slew rate of the drive circuit. Table 6 shows measured and predicted efficiency values while using the control IC and the drive stages of Fig. 6 to drive an ideal capacitive load with a sinusoidal drive signal. Finally, when attached to a piezoelectric actuator, the control IC successfully flaps the wings of the MAV of Fig. 1. High-speed video frames of wing motion from a sinusoidal V_{CTRL} signal are shown in Fig. 17.

5. Summary

This work describes optimized circuit topologies, efficient control methods, lightweight magnetic components, and circuit assembly techniques for high-voltage piezoelectric drive circuits in microrobotics. These building blocks enable power electronics packages that can meet the weight and power requirements of even the most demanding microbotic platforms, such as flapping-wing MAVs (Fig. 18), and therefore help to eliminate one of the major obstacles to the widespread use of piezoelectric actuators in low mass embedded or mobile applications. The growing range of commercially available chip-scale semiconductors, as well as improvements in the manufacturing process of miniature magnetic components, will present additional opportunities for weight reduction and efficiency improvement in the power circuits.

Acknowledgements

The authors gratefully acknowledge support from the Wyss Institute for Biologically Inspired Engineering and the National Science Foundation (award number CCF-0926148).

References

- [1] R.J. Wood, E. Steltz, R.S. Fearing, Optimal energy density piezoelectric bending actuators, *Sensors & Actuators A: Physical* 119 (2) (2005) 476–488.

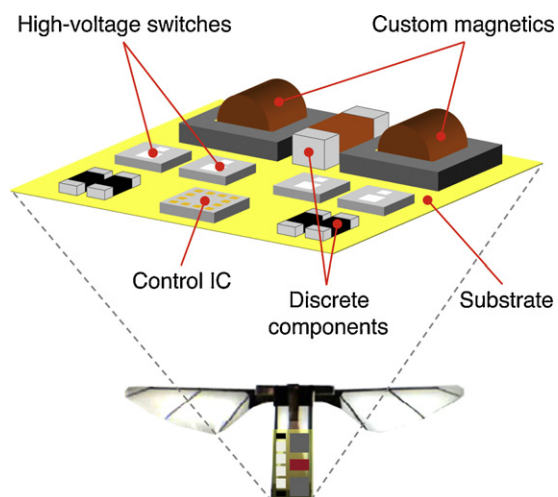


Fig. 18. Conceptual illustration of a mg-scale power electronics package suitable for onboard testing in a flapping-wing platform.

- [2] R.J. Wood, Liftoff of a 60 mg flapping-wing MAV, in: IEEE/RSJ Int. Conf. on Intelligent Robots and Systems, 2007, pp. 1889–1894.
- [3] K. Hoffman, R.J. Wood, Towards a multi-segment ambulatory microrobot, in: IEEE Int. Conf. on Robotics and Automation, Anchorage, AK, 2010, pp. 1196–1202.
- [4] A.T. Baisch, R.J. Wood, Design and fabrication of the harvard ambulatory micro-robot, in: 14th Int. Symp. of Robotics Research, 2009.
- [5] E. Steltz, M. Seeman, S. Avadhanula, R.S. Fearing, Power electronics design choice for piezoelectric microrobots, in: IEEE/RSJ Int. Conf. on Intelligent Robots and Systems, 2006, pp. 1322–1328.
- [6] D. Campolo, M. Sitti, R.S. Fearing, Efficient charge recovery method for driving piezoelectric actuators with quasi-square waves, IEEE Trans. Ultrasonics, Ferroelectrics, Frequency Control 50 (March (3)) (2003) 237–244.
- [7] B. Edamana, K. Oldham, Optimal on-off controller with charge recovery for thin-film piezoelectric actuators for an autonomous mobile micro-robot, in: Proc. of the American Controls Conference, San Francisco, CA, 2011.
- [8] W.M. Zavis, W.E. Shanks, Design advances for high-efficiency regenerative piezoelectric drive amplifier, Proc. SPIE 4327 (2001) 118–124.
- [9] D.J. Clingman, M. Gamble, High voltage switching piezo drive amplifier, Proc. SPIE 3674 (1999) 280–286.
- [10] J. Luan, Design and development of high-frequency switching amplifiers used for smart material actuators with current-mode control, Master's thesis, Virginia State University, 1998.
- [11] G. Gnad, R. Kasper, Power drive circuits for piezoelectric actuators in automotive applications, IEEE Int. Conf. on Industrial Technology 159 (2006) 7–1600.
- [12] S. Sherrit, H.D. Wiederick, B.K. Mukherjee, Accurate equivalent circuits for unloaded piezoelectric resonators, in: IEEE Ultrasonics Symposium, 1997, pp. 931–935.
- [13] M. Guan, W.-H. Lao, Studies on the circuit models of piezo-electric ceramics, in: Int. Conf. on Information Acquisition, 2004, pp. 26–31.
- [14] A. Püttmer, P. Hauptmann, R. Lucklum, O. Krause, B. Henning, SPICE models for lossy piezoceramics transducers, IEEE Trans. Ultrasonics, Ferroelectrics, Frequency Control 44 (1997) 60–66.
- [15] R.S. Dahiya, M. Valle, G. Metta, L. Lorenzelli, SPICE model of lossy piezoelectric polymers, in: IEEE Int. Symp. on the Applications of Ferroelectrics, 2008, pp. 1–4.
- [16] B.M. Finio, N.O. Pérez-Arancibia, R.J. Wood, System identification, modeling, and optimization of an insect-sized flapping-wing micro air vehicle, in: IEEE/RSJ Int. Conf. on Intelligent Robots and Systems, IROS, 2011.
- [17] Q. Wang, X. Du, B. Xu, L. Cross, Electromechanical coupling and output efficiency of piezoelectric bending actuators, IEEE Trans. Ultrasonics, Ferroelectrics Freq. Control 46 (May) (1999) 638–646.
- [18] N. Vazquez, L. Estrada, C. Hernandez, E. Rodriguez, The tapped-inductor boost converter, in: IEEE Int. Symposium on Industrial Electronics, 2007.
- [19] M. Karpelson, G.-Y. Wei, R.J. Wood, Milligram-scale high-voltage power electronics for piezoelectric microrobots, in: IEEE Int. Conf. on Robotics and Automation, 2009, pp. 883–890.
- [20] H. Janocha, C. Stiebel, New approach to a switching amplifier for piezoelectric actuators, in: Actuator 98, 1998, pp. 189–192.
- [21] K. Venkatesan, Current mode controlled bidirectional flyback converter, in: IEEE Power Electronics Specialists Conf., 1989, pp. 835–842.
- [22] M. Karpelson, J.P. Whitney, G.-Y. Wei, R.J. Wood, Design and fabrication of ultralight high-voltage power circuits for flapping-wing robotic insects, in: Applied Power Electronics Conf., 2011, pp. 2070–2077.
- [23] A.C. Tam, W.P. Leung, D. Krajnovich, Excimer laser ablation of ferrites, Journal of Applied Physics 69 (4) (1991) 2072–2075.
- [24] A. Pressman, Switching Power Supply Design, McGraw-Hill Professional, 1998.
- [25] G. Fengxun, M. Yanqiu, A universal estimating and measurement method of EMI, in: Int. Symposium on Microwave, Antenna, Propagation and EMC Technologies for Wireless Communications, 2007, pp. 1239–1242.